

4

Neutrino Oscillations

4.1

Preliminaries

A broad class of experimental data indicates that there are three neutrinos that participate in weak interactions: ν_e , ν_μ and ν_τ . From the precise measurement of the invisible width of the Z-boson at the electron–positron collider (LEP), we also know that the number of isodoublet ‘active’ neutrino flavours is exactly 3 [21]. We have also seen that massive neutrinos, in general, mix in the charged current (CC) weak interaction. This mixing implies the existence of a quantum mechanical phenomenon whereby a neutrino produced with a specific flavour (electron, muon or tau) can later be measured as having a different flavour, as illustrated in Figure 4.1. The experimental discovery of this new phenomenon in 1998 has started a revolution in particle physics, as it requires physics beyond the standard $SU(3)_c \otimes SU(2)_L \otimes U(1)_Y$ model, with potentially far-reaching implications for particle and astroparticle physics, as well as our understanding of the early Universe. In the following discussion of neutrino oscillations, we will tacitly assume that the lepton mixing matrix is strictly unitary, as our first approximation. Robustness of the results obtained with respect to this as well as other assumptions is discussed in Chapter 5.

4.2

Neutrino Oscillations Formalism *In Vacuo*

In order to fix the notation, we start our discussion of neutrino oscillations *in vacuo* by assuming the existence of just three active neutrinos.¹⁾ The process is illustrated in Figure 4.1a. We start from the Lagrangian in Eq. (2.16), and write the CC interaction of neutrinos as

$$\mathcal{L}_{CC} = -\frac{g}{\sqrt{2}} \bar{l}_\alpha \gamma^\mu P_L \nu_k U_{\alpha k} W_\mu^- - \frac{g}{\sqrt{2}} \bar{\nu}_k \gamma^\mu P_L l_\alpha U_{\alpha k}^* W_\mu^+, \quad (4.1)$$

1) This accounts for most of the existing neutrino oscillation data. For discussions including sterile neutrinos, see Ref. [46]

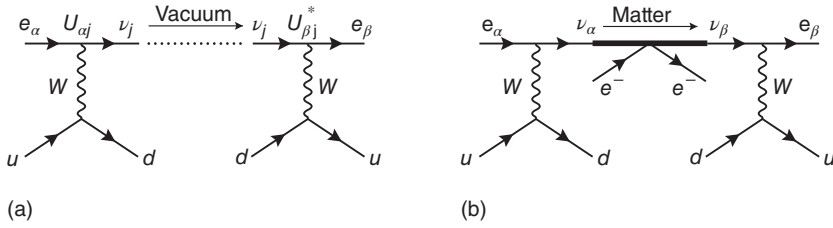


Figure 4.1 Schematic illustration of neutrino oscillations *in vacuo* (a) and in matter (b).

where

$$\nu_{\alpha L} = \sum_{i=1}^3 U_{\alpha i} \nu_{iL}, \quad (\alpha = e, \mu, \tau), \quad (4.2)$$

defines the relation between the flavour and mass eigenstates, and we have now renamed our notation as

$$K \equiv \mathbf{V}^{\text{LEP}} \equiv U,$$

in order to indicate that it is now assumed to be unitary. Note that Eq. (4.2) implies that our (standard) convention is opposite to that employed in the definition of the CKM (Cabibbo–Kobayashi–Maskawa) matrix describing quark mixing. We parameterize U in the usual way:

$$U = \begin{bmatrix} 1 & 0 & 0 \\ 0 & c_{23} & s_{23} \\ 0 & -s_{23} & c_{23} \end{bmatrix} \begin{bmatrix} c_{13} & 0 & s_{13}e^{-i\delta} \\ 0 & 1 & 0 \\ -s_{13}e^{i\delta} & 0 & c_{13} \end{bmatrix} \begin{bmatrix} c_{12} & s_{12} & 0 \\ -s_{12} & c_{12} & 0 \\ 0 & 0 & 1 \end{bmatrix} \quad (4.3)$$

$$= \begin{bmatrix} c_{12}c_{13} & s_{12}c_{13} & s_{13}e^{-i\delta} \\ -s_{12}c_{23} - c_{12}s_{23}s_{13}e^{i\delta} & c_{12}c_{23} - s_{12}s_{23}s_{13}e^{i\delta} & s_{23}c_{13} \\ s_{12}s_{23} - c_{12}c_{23}s_{13}e^{i\delta} & -c_{12}s_{23} - s_{12}c_{23}s_{13}e^{i\delta} & c_{23}c_{13} \end{bmatrix}$$

where $c_{ij} \equiv \cos \theta_{ij}$, and $s_{ij} \equiv \sin \theta_{ij}$. Two of the three angles are involved in solar and atmospheric oscillations, θ_{12} and θ_{23} , respectively. The last angle in the three-neutrino leptonic mixing matrix is θ_{13} , which has been well measured mainly by reactor experiments. This form is the same as Eq. (3.31) [46], taking $\phi_{12}, \phi_{23} \rightarrow 0$ and δ is the CP-violating phase within the PDG (Particle Data Group) convention, corresponding to the ‘invariant’ ‘Dirac phase’ combination

$$\delta \equiv \phi_{13} - \phi_{12} - \phi_{23}$$

relevant for us here (see Problem 4.2).

With the conventions of Eq. (4.2), the state vectors $|\nu_{\alpha}\rangle$ ($\alpha = e, \mu, \tau$) for flavour and $|\nu_i\rangle$ ($i = 1, 2, 3$) for mass eigenstates are related through (Problem 4.1)

$$|\nu_{\alpha}\rangle = \sum_{i=1}^3 U_{\alpha i}^* |\nu_i\rangle, \quad (\alpha = e, \mu, \tau), \quad (4.4)$$

where, for simplicity, we have omitted the subscript L which indicates the left-handed chirality.

The neutrino oscillation amplitude *in vacuo* can be written immediately by reading off the scheme in Figure 4.1a. It is then straightforward to compute the $\nu_\alpha \rightarrow \nu_\beta$ oscillation probability, which is given, for ultra-relativistic neutrinos, by

$$\begin{aligned}
 P(\nu_\alpha \rightarrow \nu_\beta) &= \left| \sum_j U_{\alpha j}^* U_{\beta j} e^{-i \frac{m_j^2}{2E} L} \right|^2 \\
 &= \delta_{\alpha\beta} - 4 \sum_{i>j} \Re(U_{\alpha i}^* U_{\alpha j} U_{\beta i} U_{\beta j}^*) \sin^2 \left(\frac{\Delta m_{ij}^2}{4E} L \right) \\
 &\quad + 2 \sum_{i>j} \Im(U_{\alpha i}^* U_{\alpha j} U_{\beta i} U_{\beta j}^*) \sin \left(\frac{\Delta m_{ij}^2}{2E} L \right), \quad (4.5)
 \end{aligned}$$

where E is the neutrino energy, L is the distance travelled by the neutrino and $\Delta m_{ij}^2 \equiv m_i^2 - m_j^2$ (m_i being mass eigenvalues) are the mass squared differences. Here, \Re and \Im denote the real and imaginary parts.

In the approximation in which only two neutrinos participate in the oscillation, the conversion probability takes a very simple form

$$P_{\text{vacuum}}(\nu_e \rightarrow \nu_\mu) = \sin^2(2\theta) \sin^2 \left(\frac{\Delta m^2 L}{4E} \right), \quad (4.6)$$

where Δm^2 is the neutrino mass squared difference and θ the corresponding mixing angle. This leads to a very simple pattern illustrated in Figure 4.2. The solid curve shows the probability for the original neutrino retaining its identity, while the dashed one shows the probability of conversion to the other neutrino species. The maximum probability of conversion is $\sin^2 2\theta$, and the frequency of the oscillation is controlled by Δm^2 .

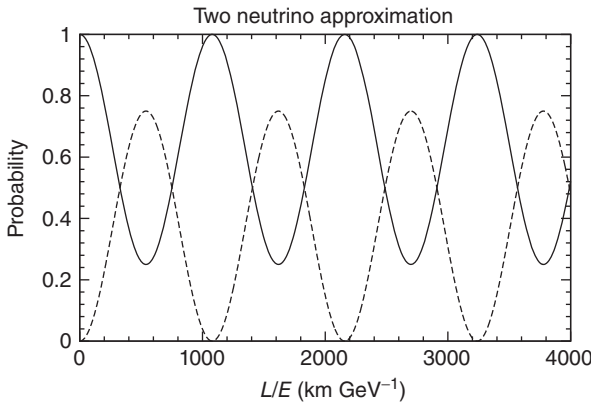


Figure 4.2 Schematic illustration of two-neutrino survival and conversion oscillation probabilities *in vacuo*.

The quantities appearing inside the arguments of the oscillating functions, namely

$$L_{ij}^{\text{osc}} \equiv 2\pi \frac{2E}{\Delta m_{ij}^2}, \quad (4.7)$$

are called *neutrino oscillation lengths*. One sees that neutrino oscillations are present only if the mixing matrix U has some non-vanishing non-diagonal matrix elements and the neutrino masses are non-degenerate. In other words, each of the three neutrino flavour states which interact with the charged leptons in weak interactions is a different superposition of the three neutrino states of definite mass.

Neutrinos are created in weak decays and reactions as flavour eigenstates. As a neutrino propagates through space, the quantum mechanical phases of the three mass states evolve at slightly different rates because of the small light neutrino mass differences. This results in a changing mixture of mass states as the neutrino travels. Of course, a different mixture of mass states corresponds to a different mixture of flavour states. Hence, a neutrino born, say, as an electron neutrino will become a mixture containing muon and tau neutrinos after travelling some distance. Since the quantum mechanical phase evolves in a periodic way, after some distance the state will nearly return to the original mixture, and the neutrino will be again mostly an electron neutrino. The flavour content of the neutrino will then continue to oscillate as long as the quantum mechanical state maintains coherence. Since the mass differences between the neutrinos are very small, the coherence length for neutrino oscillations will be very long, making this microscopic quantum effect observable over macroscopic distances.

One sees also that the oscillation arises from an interference between the different mass eigenstates in the neutrino wave function. Oscillations do not probe the neutrino masses themselves, but rather the squared mass splittings which appear in the oscillation length. Information on the mixing coefficients is obtained from the oscillation amplitudes. The oscillation pattern depends on L/E , the ratio of the distance to the neutrino energy. In an actual experiment, both the L dependence and the E dependence can be used to explore various types of oscillations. Typical values of L/E for different types of neutrino sources and experiments are summarized in Figure 4.3. In order to be sensitive to a given value of Δm^2 , the experiment

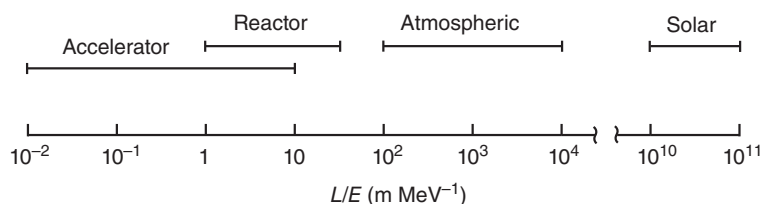


Figure 4.3 Schematic illustration of the L/E value characterizing various types of neutrino oscillation experiments.

Table 4.1 Typical L and E values for various neutrino sources and oscillation experiments and the corresponding Δm^2 sensitivity ranges.

Experiment		L (m)	E (MeV)	Δm^2 (eV ²)
Solar		10^{10}	1	10^{-10}
Atmospheric		$10^4 - 10^7$	$10^2 - 10^5$	$10^{-1} - 10^{-4}$
Reactor	SBL	$10^2 - 10^3$	1	$10^{-2} - 10^{-3}$
	LBL	$10^4 - 10^5$		$10^{-4} - 10^{-5}$
Accelerator	SBL	10^2	$10^3 - 10^4$	> 0.1
	LBL	$10^5 - 10^6$	10^4	$10^{-2} - 10^{-3}$

must have $E/L \approx \Delta m^2 (L \sim L_{ij}^{\text{osc}})$. The corresponding ranges of Δm^2 to which these experiment types can be most sensitive are summarized in Table 4.1.

There are two main ways to probe for neutrino oscillations, namely ‘appearance’ and ‘disappearance’ experiments. In the first case, one starts with a beam of neutrinos of a given flavour and observes neutrinos of a different flavour after they travel a distance L from the neutrino source. If oscillations are present, the oscillation probability to the different flavour is non-vanishing. In this case, one needs a neutrino beam of energy larger than the rest mass of the charged lepton to be created in the detection reaction.

In ‘disappearance’ experiments, the detector is sensitive to the same flavour of the neutrinos as originally present in the beam. If oscillations are present, the ‘survival’ probability is smaller than unity. In these experiments, one probes oscillations from the original flavour to all others, and hence it is an ‘inclusive’ approach.

In order for neutrino oscillations to occur, the neutrinos with definite flavour $|\nu_\alpha\rangle$ ($\alpha = e, \mu, \tau$) must not be mass eigenstates, but linear combinations of them. However, neutrino oscillations can be observed only if the neutrino production, propagation and detection coherence conditions are satisfied.

The production and detection coherence conditions ensure that the intrinsic quantum mechanical energy uncertainties at neutrino production and detection are large with respect to the energy difference of different neutrino mass eigenstates. The intrinsic spread in the neutrino beam’s momentum leads to an uncertainty in the momentum, which is taken into account explicitly within a wave packet description of neutrino oscillations [3, 189–191]. For the case of ultra-relativistic neutrinos, one finds that the coherence length has the upper bound [191]

$$L_{ij}^{\text{coh}} \lesssim E [L_{ij}]^2 = \frac{16\pi^2 E^3}{[\Delta m_{ij}^2]^2} \quad (4.8)$$

beyond which the coherence length loses its meaning.²⁾ For distances less than many oscillation lengths, one finds that the wave packet treatment gives the same results as the standard one.

2) We note that the neutrino oscillation coherence conditions give upper limits on the mass squared differences of different neutrino mass eigenstates.

On the other hand, propagation decoherence can take place if neutrinos propagate over very long distances. It relates to the fact that the wave packets describing different neutrino mass eigenstates that make up a flavour state propagate with different group velocities, and therefore after a long enough time they can separate so much that the amplitudes of their interaction with the detector particles can no longer produce interference. The separation of the mass eigenstate neutrinos from each other as a neutrino beam travels large distances from its source leads to loss of interference. Once the mass eigenstates have separated, the difference between their arrival times at the detector may be observable. However, as long as the dimensions of the region within which the neutrino's parent is effectively localized are macroscopic, the loss of coherence will not occur until oscillations have already been washed out by the broad momentum spread in any realistic neutrino experiment. For neutrinos with mass in the electronvolt range, coherence is certainly lost in the case of extra-terrestrial neutrinos such as solar neutrinos, in which case what arrives at the underground detector on Earth is an incoherent neutrino admixture. In other words, solar neutrino oscillations do not take place through vacuum.

4.3

Matter Effects in Neutrino Oscillations

So far we have considered only neutrino oscillations in vacuum. In order to discuss actual neutrino oscillation experiments, one must take matter effects into account. This is clear for the case of solar neutrinos, as these are produced in the interior of the Sun and must traverse the solar interior as well as Earth matter before being detected in underground experiments such as Super-Kamiokande. Similarly, Earth matter effects are relevant for the study of atmospheric and, to some extent, also long-baseline oscillation experiments. For an extensive discussion of this subject, see, for example Ref. [192]. Here we just give a very brief summary of what is used in data handling.

Neutrinos passing through matter will interact with the particles in the medium, like the Sun. The presence of electrons in the medium changes the energy levels of the mass eigenstate neutrinos because of CC coherent forward scattering of the electron neutrinos. This effect comes from the diagrams illustrated in Figure 4.4 and must be taken into account when considering the oscillations of neutrinos travelling through matter [59].

This means that neutrinos in matter have an effective mass different from that in vacuum, and since neutrino oscillations depend upon neutrino squared mass differences, they may be different in matter than they are in vacuum. This can be neatly described in terms of effective potentials $V(x)$, as illustrated in the right panel in Figure 4.1. For an unpolarized medium,³⁾ this potential is given as

$$V(x) = \sqrt{2}G_F N_e(x), \quad (4.9)$$

3) Neutrino evolution in polarized media may be relevant in other astrophysical situations, see Ref. [193].

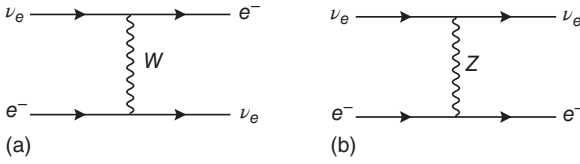


Figure 4.4 (a,b) Feynman diagrams for neutrino interactions with electrons in matter.

where G_F is the Fermi constant, and $N_e(x)$ is the electron number density at x . For example, taking into account the values of the electron density in the neutrino-producing region of the Sun, say from the core up to $0.3R_\odot$, where R_\odot is the solar radius, one finds that the numerical value of this potential V varies from 8×10^{-12} eV to 8×10^{-13} eV or so. Comparing with the inverse oscillation length *in vacuo* $\Delta m_\odot^2/E$ obtained in global neutrino oscillation fits, one sees that it could be of the same order of magnitude as V for high-energy solar neutrinos, such as ^8B neutrinos. This way, one can understand, *a posteriori*, that the presence of this matter potential may substantially modify effective ‘masses’ and mixing angles inside the solar medium. In fact, one can show that, for example, within the adiabatic regime of slowly varying matter densities, the mixing angle in matter is given by the Mikheyev–Smirnov–Wolfenstein (MSW) expression [59, 60]

$$\cos 2\theta_m = \frac{\Delta m^2 \cos 2\theta - 2\sqrt{2} EG_F N_e}{\sqrt{(\Delta m^2 \cos 2\theta - 2\sqrt{2} EG_F N_e)^2 + (\Delta m^2 \sin 2\theta)^2}}. \quad (4.10)$$

This clearly illustrates the possibility of resonant amplification of neutrino mixing as a result of including matter effects [60].

What is ultimately relevant in order to describe the experimental data is the so-called neutrino survival probability, illustrated in Figure 4.5. One sees that the effect of matter is, indeed, more important for the suppression of high-energy

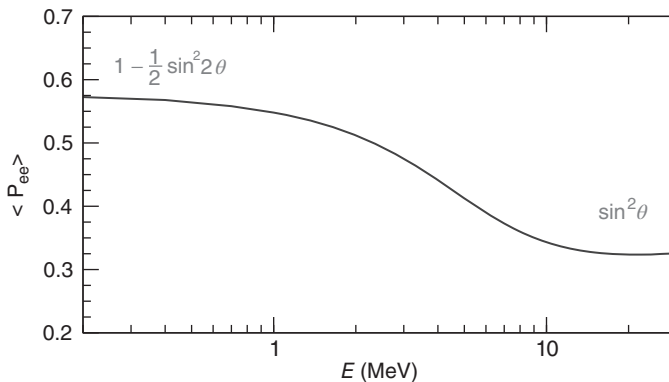


Figure 4.5 Average ^8B solar neutrino survival probability versus energy for best fit oscillation parameters [83]. Matter effects are important for high-energy neutrinos, while low-energy neutrinos are suppressed as *in vacuo*. (Courtesy of M. Tórtola.)

solar neutrinos than it is for the low-energy part of the solar neutrino spectrum. For high-energy solar neutrinos, one finds a stronger suppression in the flux reaching the detectors, as indicated by the data (see below).

The neutrino evolution equation in matter is described in terms of neutrino flavour eigenstates as

$$i \frac{d}{dx} \begin{bmatrix} \nu_e \\ \nu_\mu \\ \nu_\tau \end{bmatrix} = H(x) \begin{bmatrix} \nu_e \\ \nu_\mu \\ \nu_\tau \end{bmatrix}, \quad (4.11)$$

where ν_α ($\alpha = e, \mu, \tau$) is the amplitude for the α flavour. The Hamiltonian matrix H is given by

$$H(x) = U \begin{bmatrix} \frac{m_1^2}{2E} & 0 & 0 \\ 0 & \frac{m_2^2}{2E} & 0 \\ 0 & 0 & \frac{m_3^2}{2E} \end{bmatrix} U^\dagger + \begin{bmatrix} V(x) & 0 & 0 \\ 0 & 0 & 0 \\ 0 & 0 & 0 \end{bmatrix}, \quad (4.12)$$

where x is the position along the neutrino path and $V(x)$ is the matter potential given in Eq. (4.9). The Hamiltonian matrix in Eq. (4.12) can be replaced by

$$H(x) = U \text{diag} \left[0, \frac{\Delta m_{21}^2}{2E}, \frac{\Delta m_{31}^2}{2E} \right] U^\dagger + \text{diag}[V(x), 0, 0] \quad (4.13)$$

by re-phasing all of the neutrino flavours by $\exp[-im_1^2 x/(2E)]$. For anti-neutrinos, the same equation holds with the change $V(x) \rightarrow -V(x)$ and $U \rightarrow U^*$ (or equivalently $\delta \rightarrow -\delta$). At a given point x , the Hamiltonian can be diagonalized by using the effective mixing matrix in matter, $U(N)$:

$$H(x) = U(x) \text{diag} \left[0, \frac{\Delta m_{21}^2(N)}{2E}, \frac{\Delta m_{31}^2(N)}{2E} \right] U^\dagger(x), \quad (4.14)$$

where $\Delta m_{ij}^2(x)$ are the effective mass squared differences in matter.

Before concluding this section, let us note that, since the neutral current (NC) scattering is diagonal and does not distinguish between neutrino flavours, it just causes an overall phase shift of no physical importance as it drops out in Eq. (4.12).⁴⁾ This follows from the assumption of unitarity of the lepton mixing matrix and consequent triviality of the NC, see Eq. (3.38). These features can be broken appreciably in low-scale seesaw-type schemes. In this case, the NC would also contribute relevant potentials to be taken into account in the neutrino evolution equation. In such a case, in addition to matter effects associated with the CC [59, 60], those related to NC [55] are also necessary to describe neutrino propagation in very dense media such as supernovae. In fact, under certain circumstances, massless neutrinos would be able to undergo resonant conversion as a result of such non-standard NC form [55]. While this has no relevant effect for the propagation of solar neutrinos, it may have important implications in astrophysics involving the propagation of supernova and pulsar neutrinos [56, 57, 195].

4) There are, however, small calculable radiative corrections to neutrino indices of refraction [194].

4.4

Neutrino Oscillation Data

Neutrinos are characterized by their weak interactions, arising from a variety of processes such as beta decays in atomic nuclei. They are produced by natural sources like the Sun, from the interaction of cosmic rays with atomic nuclei in the Earth's atmosphere and in the laboratory as accelerator beams and from nuclear reactors. A new generation of experiments including Super-K, the Sudbury Neutrino Observatory (SNO), KamLAND and accelerators has shown that neutrino flavours get inter-converted during their propagation mainly by the mechanism of oscillations.

4.4.1

Solar Neutrino Data

The Sun sends enormous numbers of neutrinos in all directions, arising from the thermonuclear reactions that take place in its interior and which generate the solar energy. These reactions occur via two main chains: the pp chain and the CNO (carbon–nitrogen–oxygen) cycle. There are five reactions that produce ν_e in the pp chain and three in the CNO cycle. Their net result is that, when four protons merge to become a ${}^4\text{He}$ nucleus, two of them convert into neutrons, each such conversion releasing one electron neutrino:

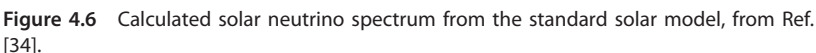


where the energy released in the reaction, $Q \simeq 26$ MeV, is mostly radiated through the photons and only a small fraction is carried by the neutrinos, $\langle E_{2\nu_e} \rangle = 0.59$ MeV.

Since the pioneering experiment of Ray Davis, physicists were puzzled by the discrepancy between solar neutrino measurements and the expectations based upon the standard solar model (SSM) flux calculations [34], as illustrated in Figure 4.6. Such solar neutrino puzzle can be understood if the electron neutrinos produced in the Sun would get transformed into other flavours that the experiments could not detect.

Solar neutrino data have been collected in a variety of experiments, including the rates of the radiochemical experiments, namely the chlorine [33] ($2.56 \pm 0.16 \pm 0.16$ SNU),⁵⁾ as well as the gallium experiments SAGE [196] ($66.9^{+3.9}_{-3.8} {}^{+3.6}_{-3.2}$ SNU) and GALLEX/GNO [197] ($69.3 \pm 4.1 \pm 3.6$ SNU). The zenith angle dependence and recoil energy spectrum of solar neutrinos have been recorded by the Super-Kamiokande experiment in the three phases of the experiment [198–200].

5) One solar neutrino unit (SNU) is defined as the neutrino flux producing 10^{-36} captures per target atom per second in radiochemical neutrino experiments.


$$\nu_\alpha + e^- \rightarrow \nu_\alpha + e^- \quad (4.16)$$
$$\nu_e + d \rightarrow p + p + e^- \quad (4.17)$$
$$v_\alpha(\bar{v}_\alpha) + d \rightarrow v_\alpha(\bar{v}_\alpha) + p + n. \quad (4.18)$$

6) In order to make use of this reaction, background neutrons from natural radioactivity and from cosmic ray muons had to be brought to the minimum, taking advantage of the great depth of the SNO facility, two kilometres below the surface.

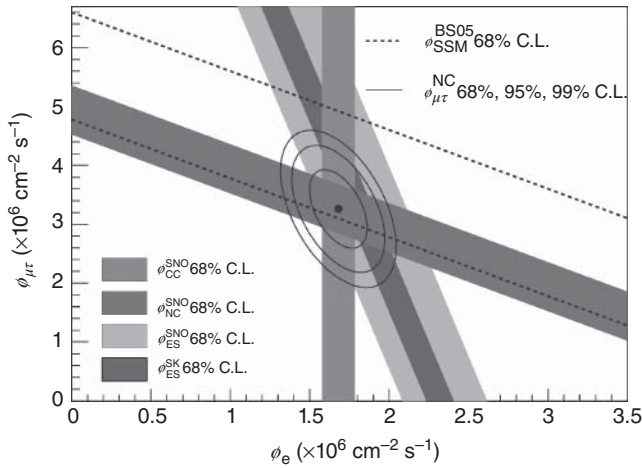


Figure 4.7 The SNO CC, ES and NC and Super-Kamiokande ES constraints on the ν_e and ν_{τ} components of the ^8B flux. The SSM total flux is also shown. All results are

consistent with a terrestrial flux of solar neutrinos, which is about one-third ν_e s and two-thirds ν_{τ} . (Adapted from [201].)

Super-K ES results, and the predictions of the SSM 2005 are shown in Figure 4.7, taken from [201].

From the three phases of the SNO experiment, one sees that the data are consistent, showing that approximately two-thirds of the solar neutrinos arriving at Earth are heavy-flavour neutrinos. The total flux is consistent with the SSM, given the uncertainties. This provides strong evidence for solar electron neutrino ν_e flavour conversions.

Last, but not least, comes the Borexino experiment, located in the Gran Sasso Laboratory at an effective depth of about 3.0 km.w.e., the first to measure low-energy (<1 MeV) solar neutrino events in real time. The Borexino collaboration has now given a precision measurement of the ^7Be neutrino flux to within 5% [205], with an initial result also for the pep flux [206], thus providing an important confirmation of the SSM, as well as consistency with the large mixing angle (LMA) oscillations [207].

In summary, we collect in Table 4.2 the main features of the solar neutrino experiments that have been carried out to date, including their energy thresholds and the main solar neutrino fluxes to which they are sensitive ('Radio' stands for radiochemical experiment).

4.4.2

Reactor Neutrino Data

One may also search for neutrino oscillations using neutrinos from nuclear reactors. These produce $\bar{\nu}_e$ with E on the order of megaelectronvolts. Because of the

Table 4.2 Compilation of all solar neutrino experiments, from Ref. [208].

Experiment	Type	Method	Dates	Threshold (MeV)	Main fluxes
Homestake Cl	Radio	CC	1968–2002	0.811	^8B , ^7Be
Kamiokande	Active	ES	1987–1995	7.0–9.0	^8B
SAGE	Radio	CC	1990–now	0.233	pp, ^7Be
GALLEX/GNO	Radio	CC	1991–2003	0.233	pp, ^7Be
Super-K	Active	ES	1996–now	4.0–7.0	^8B
SNO	Active	ES/CC/NC	1999–2006	4.0–7.25; 2.22(NC)	^8B
Borexino	Active	ES	2008–now	~ 0.8	^7Be , pep, ^8B

low energy, e 's are the only charged leptons that can be produced in the resulting CC interactions. Should the $\bar{\nu}_e$ oscillate to another flavour, its CC interactions would be missed. Therefore, oscillation experiments performed at reactors are disappearance experiments. They tend to probe smaller values of squared mass splittings due to the lower neutrino energy.

Reactor experiments performed at relatively short or intermediate Baselines, including Gosgen [209], Krasnoyarsk [210], Bugey [211], CHOOZ [212] and Palo Verde [213], have all given no positive evidence of flavour mixing.

Smaller Δm^2 values can be probed by using a longer baseline. This has been implemented in the KamLAND experiment, currently in operation in the Kamioka mine in Japan. This employs a 1000-ton liquid scintillation counter to detect the process $\bar{\nu}_e + p \rightarrow e^+ + n$ and lies at an underground site located at an average distance of 150–210 km from a network of Japanese nuclear power stations. Here, the delayed coincidence of the prompt energy from the positron and a characteristic gamma from the neutron capture allows an efficient reduction of backgrounds. Most of the incident $\bar{\nu}_e$'s come from nuclear plants at distances of 80–350 km from the detector, far enough to probe LMA neutrino oscillations. Assuming CPT (charge conjugation, parity, time reversal) invariance, one can directly compare the information obtained from solar neutrino experiments with that arising from the KamLAND reactor results. The measurement of the flux and energy spectrum of the $\bar{\nu}_e$'s emitted by these reactors provides a test of neutrino oscillations with $\Delta m^2 \gtrsim 10^{-5} \text{eV}^2$.

The first KamLAND data corresponding to a 162-ton-year exposure gave 54 anti-neutrino events in the final sample, after cuts, whereas 86.8 ± 5.6 events are predicted for no oscillations with 0.95 ± 0.99 background events [71]. This gave the first terrestrial confirmation of oscillations at the solar mass scale. Additional KamLAND data with a larger fiducial volume of the detector corresponding to a 766.3-ton-year exposure have been presented in [214], leading to a confidence level of 99.995% for $\bar{\nu}_e$ disappearance, in addition to evidence for spectral distortion consistent with oscillations. Subsequent data [215, 216] have provided a better measurement of the solar neutrino oscillation parameters, especially the 'solar' mass-squared splitting, as a result of the reduction of systematic uncertainties thanks to the full volume calibration.

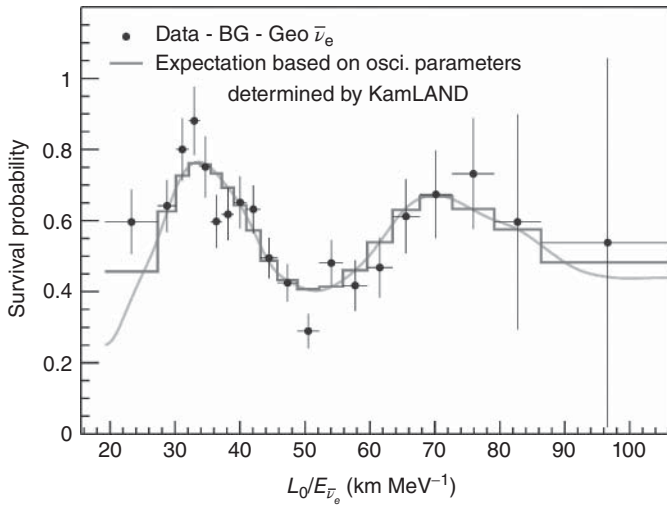


Figure 4.8 Evidence for neutrino oscillation at the solar scale in the KamLAND reactor experiment, from Ref. [215].

Figure 4.8 gives the ratio of the background and geoneutrino subtracted $\bar{\nu}_e$ spectrum to the expectation for no oscillation as a function of L_0/E , where $L_0 = 180$ km is the effective baseline taken as a flux-weighted average. The energy bins are equal-probability bins of the best fit including all backgrounds. The histogram and curve show the expectation accounting for the distances to the individual reactors, time-dependent flux variations and efficiencies. The error bars are statistical only, and do not include, for example, correlated systematic uncertainties in the energy scale. This provides evidence for neutrino oscillation at the solar mass scale in the KamLAND experiment [215].

In short, while the solar and atmospheric indications discussed in Section 4.4.1 were suggestive, indeed, of the idea of neutrino oscillation, it was crucial that they were subsequently confirmed by observations with neutrinos produced at nuclear reactors. These experiments not only gave a vital terrestrial confirmation of the solar neutrino oscillation hypothesis, ruling out solutions based on non-standard interactions [217] or magnetic transition moments [218, 219], but also established robustness of the LMA oscillation solution [72–74]. Altogether, they have contributed significantly to bringing the whole field of neutrino physics into the precision era [82].

4.4.3

Atmospheric Neutrino Data

The interactions of cosmic rays with the nitrogen and oxygen nuclei in the Earth's atmosphere at an average height of 15 km produce mostly pions and some kaons that decay into electron and muon neutrinos as well as anti-neutrinos.

Atmospheric neutrino interactions are observed in underground experiments using various techniques and lead to different event types depending on their energy. For example, they can be detected by observing their CC interaction inside the detector. These are called *contained* events. These may be fully contained (FC) when the charged lepton (either electron or muon) produced in the neutrino interaction does not escape the detector, or partially contained (PC) when the produced muon leaves the detector. For FC events, the flavour, kinetic energy and direction of the charged lepton can be best determined. Higher energy muon neutrinos and anti-neutrinos can also be detected indirectly through the muons produced in their CC interactions close to the detector wall. These are called *up-going muons*. When the muon stops inside the detector, it is called a *stopping muon*, and if the muon track crosses the full detector, the event is classified as a *through-going muon*. Down-going muons from ν_μ interactions above the detector cannot be distinguished from the cosmic ray muon background. Higher energy ν_e 's cannot be detected this way, as the produced electron showers immediately in the rock.

A collaboration of particle physicists from the Tata Institute of Fundamental Research, India, Osaka City University, Japan, and Durham University, UK, recorded the first cosmic ray neutrino interaction in an underground laboratory in Kolar Gold Fields in India in 1965. These experiments measured the flux of horizontal muons which, although not in full agreement with theoretical predictions, could not establish a statistically significant discrepancy.

Experiments originally designed to search for proton decay, for which atmospheric neutrinos constitute background, were proposed and built in the 1970s and 1980s. Two different detection techniques were employed. In water Cerenkov detectors, the target is a large volume of water surrounded by photomultiplier tubes that detect the Cerenkov ring produced by the charged leptons. Events are electron-like (muon-like) if the ring is diffuse (sharp). In iron calorimeters, the detector is made up of a set of alternating layers of iron that act as a target and some tracking element (such as plastic drift tubes), which allows the reconstruction of the shower produced by the electrons or the tracks produced by muons. Both types of detectors allow for flavour identification of the events as well as the measurement of the scattering angle of the outgoing charged lepton and some determination of its energy.

The Super-Kamioka Neutrino Detection Experiment (Super-K, for short) setup lies about 1000 m underground the Mount Kamioka area in Japan. The observatory was designed to search for nucleon decay, study solar and atmospheric neutrinos, and keep watch on supernovae in the Milky Way galaxy.

Given that ν_e is produced mainly from the decay chain $\pi \rightarrow \mu \nu_\mu$ followed by $\mu \rightarrow e \nu_\mu \nu_e$, one naively expects a 2 : 1 ratio of ν_μ to ν_e . For higher energy events, the expected ratio is larger, since some of the muons arrive on Earth before decaying.

Various atmospheric flux calculations have been performed in the last decade [220, 221], leading to absolute atmospheric neutrino flux predictions varying up the 20% level, while the flavour ratios are expected to be accurate to better than 5%. For this reason, most of the early experiments gave their results in terms of

the flavour ratio of their event rates with respect to the Monte Carlo expectation $R_{\mu/e}/R_{\mu/e}^{MC}$.

The two oldest iron calorimeter experiments, Frejus and NUSEX, found atmospheric neutrino fluxes in agreement with theory predictions. On the other hand, two water Cerenkov detectors, IMB and Kamiokande, detected a ratio of ν_μ to ν_e induced events smaller than the expected one by a factor of about 0.6, finding an atmospheric neutrino ‘anomaly’. However, the fact that the anomaly was present only in water Cerenkov detectors and not in iron calorimeters left room for the suspicion of a possible systemic problem as the origin of the effect.

Kamiokande also presented the zenith angular dependence of the deficit for the multi-gigaelectronvolt neutrinos. The zenith angle, parameterized in terms of $\cos \theta$, measures the direction of the reconstructed charged lepton with respect to the vertical of the detector. Vertically down-going (up-going) particles correspond to $\cos \theta = +1(-1)$. Horizontal particles come at $\cos \theta = 0$. The Kamiokande results seemed to indicate that the deficit was mainly due to the neutrinos coming from below the horizon. Atmospheric neutrinos are produced isotropically at about 15 km above the Earth’s surface. Hence neutrinos coming from the top of the detector travel approximately 15 km before interacting, while those coming from the bottom of the detector traverse the full diameter of the Earth, $\sim 10^4$ km, before reaching the detector. The Kamiokande distribution suggested that the deficit increased with the distance between the neutrino production and interaction points.

Atmospheric neutrino measurements at the Super-K water Cerenkov experiment [75] have confirmed earlier hints based on rate measurements, recording less atmospheric neutrinos than expected (see Ref. [82] for extensive experimental References). The Super-K CC atmospheric neutrino events include the e -like and μ -like data samples of sub- and multi-GeV contained events arranged in zenith-angle bins. Moreover, in 2004 a detailed analysis of atmospheric neutrinos was performed by the Super-K collaboration, observing a dip in the L/E distribution of the atmospheric ν_μ survival probability [222].

It was the zenith angle dependence of the μ -like atmospheric neutrino data that in 1998 gave the first evidence for neutrino oscillations. Atmospheric neutrino data are categorized into FC, PC, and upward-going muons (UP_μ). In the FC events, all of their Cerenkov light is deposited in the inner detector (ID). In the PC events, there is an exiting particle that deposits visible energy in the outer detector (OD). Figure 4.9 gives the zenith angle distributions of FC e -like, μ -like, PC, and UP_μ data denoted by filled circles with statistical error bars. Monte Carlo distributions without oscillation (boxes) and for best fit distributions (dashed) are given. The non-oscillated Monte Carlo shows the distribution without fitting, and the box height shows the statistical error. For the case of non-zero θ_{13} , matter enhanced excess of electron-like events is expected in the zenith angle of $-1 < \cos \theta < -0.2$ regions in the multi-GeV single-ring and multi-ring electron-like samples. The ν_μ in the resonance regions populate mainly in the multi-GeV single-ring muon, multi-ring muon, two PC, and UP-stopping μ samples [223].

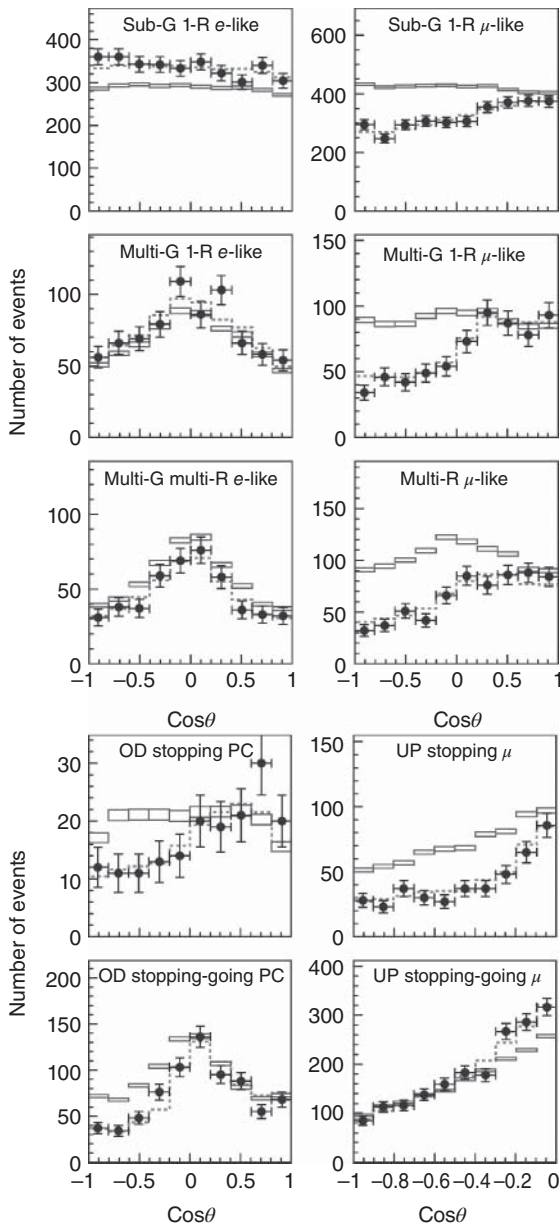


Figure 4.9 Zenith angle distributions of various atmospheric neutrino event data samples. Data are indicated by circles with statistical error bars. Boxes represent the no-oscillation standard model prediction, while

dashed histograms indicate the best fit oscillation hypothesis expectations. (Reprinted from Ref. [223] to which the reader is addressed for details.)

Altogether, the signature for atmospheric neutrino oscillations has by now become overwhelming. Indeed, the data now exclude non-oscillatory solutions to the atmospheric 'anomaly', for example, those based on non-standard neutrino interactions [224] which were quite viable at the very beginning of atmospheric data collection. Such NSI-based conversions can now be present only at a sub-leading level [82, 225].

4.4.4

Accelerator Neutrino Data

The disappearance of ν_μ 's over a long baseline probing the same Δm^2 region relevant for atmospheric neutrinos is now available from accelerator neutrino oscillation experiments, such as the KEK to Kamioka (K2K) neutrino oscillation experiment, the MINOS experiment using the NuMI beam-line facility at Fermilab and also the T2K (Tokai to Kamioka) experiment in Japan. Neutrinos produced by a 12-GeV proton beam from the KEK proton synchrotron consist of 98% muon neutrinos with a mean energy of 1.3 GeV. The beam is controlled by a near detector (ND) 300 m away from the proton target. Comparing these ND data with the ν_μ content of the beam observed by the Super-K detector at a distance of 250 km gives information on neutrino oscillations. The K2K collaboration has published details of the analysis of their full data sample (K2K-I and K2K-II) [226]. The data have been taken in the period from June 1999 to November 2004 and correspond to 0.922×10^{20} POT (protons on target). Without oscillations, $158^{+9.2}_{-8.6}$ events are expected, whereas only 112 events have been observed. Out of these, 58 events are single-ring events where the reconstruction of the neutrino energy is possible. These events have been used to perform a spectral analysis of the K2K data, as described in Ref. [82]. The first MINOS results were released in 2006 [77]. MINOS is a long-baseline experiment that searches for ν_μ disappearance in a neutrino beam with a mean energy of 3 GeV produced at Fermilab. The ND is located at 1 km from the neutrino source, and the far detector is at the Soudan Mine, at 735 km from Fermilab. The first data corresponding to 0.93×10^{20} POT, had a comparable weight to the final K2K data sample, providing a 5.0σ evidence for neutrino disappearance. Additional data by the MINOS Collaboration have been reported in Refs [227–230]. Most recently reported measurements comprise exposures of 10.71×10^{20} POT in the ν_μ -dominated beam, 3.36×10^{20} POT in the $\bar{\nu}_\mu$ -enhanced beam and 37.88 kton-years of atmospheric neutrinos. Assuming identical ν and $\bar{\nu}$ oscillation parameters, the collaboration makes a determination of oscillation parameters from ν_μ and $\bar{\nu}_\mu$ disappearance using beam and atmospheric data from MINOS [231]. In particular, the L/E shape of their data gives a strong indication for neutrino oscillations, as shown in Figure 4.10.

To conclude, we mention that recently the T2K Collaboration has published, in addition to ν_μ disappearance data, an independent indication of electron neutrino appearance from an off-axis high-intensity muon neutrino beam produced at the proton accelerator facility J-PARC [79].

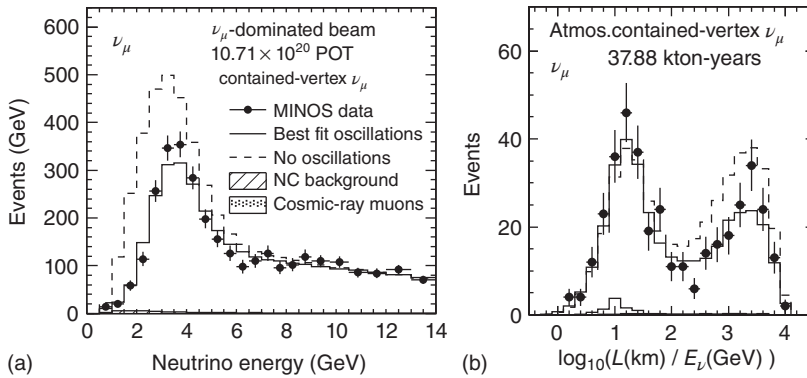


Figure 4.10 (a,b) Evidence for neutrino oscillation at the atmospheric scale in the MINOS accelerator experiment, from Ref. [231].

4.4.5

The Measurement of θ_{13}

For a long time, the most sensitive measurements of reactor anti-neutrinos were reported by the CHOOZ [212] and Palo Verde [213] experiments. In 2012, in chronological order, the Double Chooz (DC) [232], Daya Bay (DYB) [78] and RENO [233] collaborations reported measurements of the electron anti-neutrino disappearance with important levels of statistical significance. All these experiments look for the disappearance of reactor anti-neutrinos over baselines of about 1 km due to neutrino oscillations mainly driven by the third mixing angle θ_{13} of the lepton mixing matrix in Eq. (4.3). Compared to the earlier experiments, these have larger statistics, thanks to their increased reactor power and the bigger anti-neutrino detector size. Moreover, they have detectors located at different distances from the reactor core. As a result, measurements at the closest detectors can be used to predict the expected event number at the more distant detectors, avoiding the need to rely on theoretical calculations of the produced anti-neutrino flux at the reactors.

DC is a reactor experiment located in France, planned to have two detectors and two reactors. In its first stage, DC has reported 101 days of running [232], with only the far detector. The ND is expected to start collecting data soon. The two reactors are approximately equal, with an individual power of $4.25 \text{ GW}_{\text{th}}$ and placed at a distance of 1050 m from the far detector, which has a fiducial volume of 10 m^3 of neutrino target liquid. From the analysis of the rate and the energy spectrum of the prompt positrons produced by the reactor anti-neutrinos, the DC collaboration finds $\sin^2 2\theta_{13} = 0.086 \pm 0.041(\text{stat}) \pm 0.030(\text{syst})$. Using only the ratio of the observed to the expected events, they get a slightly higher best fit value: $\sin^2 2\theta_{13} = 0.104 \pm 0.030(\text{stat}) \pm 0.076(\text{syst})$. A more recent analysis of DC data with an exposure of 227.93 live days [234] has reported the observation of 8249 candidate electron anti-neutrinos while 8937 were expected if $\theta_{13} = 0$. Using a

rate plus spectral shape analysis, the following best fit value for the reactor angle is obtained: $\sin^2 2\theta_{13} = 0.109 \pm 0.030(\text{stat}) \pm 0.025(\text{syst})$.

The DYB reactor experiment in China [78] is a neutrino oscillation experiment designed to measure the mixing angle θ_{13} as well. The experiment contains an array of three groups of detectors and three groups of two reactor cores. The far group of detectors (far hall) is composed of three detectors, and the two near halls are composed by one and two detectors, respectively. In order to reduce systematic errors, the detectors are approximately equal, with a volume of 20 tons of gadolinium-doped liquid scintillator as neutrino target material. The reactor cores are approximately equal as well, and the detector separations range from 350 to 2000 m approximately. The results of the rate-only analysis performed by the DYB collaboration are illustrated in Figure 4.11.

The error bar includes statistical, detector-related and background-related uncertainties. The oscillation survival probability at the best fit value is given by the smooth curve. The χ^2 function versus $\sin^2 2\theta_{13}$ is shown in the insert. One finds a best fit value of $\sin^2 2\theta_{13} = 0.092 \pm 0.016(\text{stat}) \pm 0.005(\text{syst})$, with a zero value for θ_{13} excluded with a significance of 5.2σ .

The RENO experiment [233] is located in South Korea, with some common features with DC and DYB. RENO has six reactor cores distributed along a 1.3-km straight line. Reactor anti-neutrinos are detected by two identical detectors, labelled as near and far, located at 294 and 1383 m from the reactor array centre. Each RENO detector contains 16 tons of gadolinium-doped liquid scintillator. Based on a rate-only analysis of a 229-day run, the RENO collaboration finds

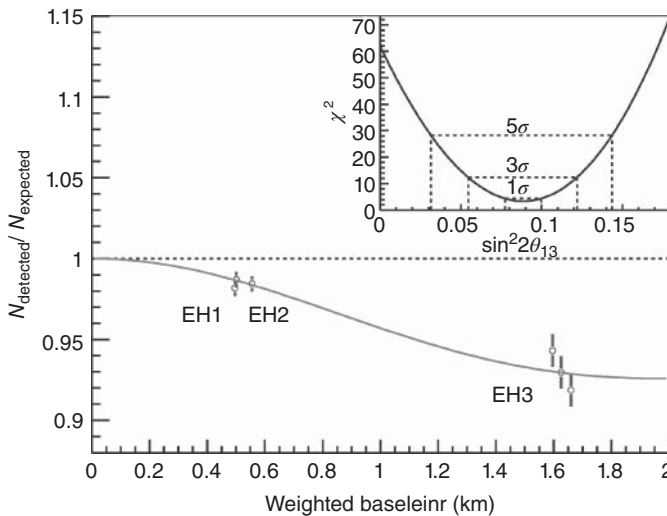


Figure 4.11 Ratio of measured versus expected signal in each Daya Bay reactor detector, assuming no oscillation. χ^2 versus $\sin^2 2\theta_{13}$ is shown in the top-right panel. (Adapted from Ref. [78].)

$\sin^2 2\theta_{13} = 0.113 \pm 0.013(\text{stat.}) \pm 0.019(\text{cyst.})$, together with a 4.9σ exclusion for $\theta_{13} = 0$.

There have also been earlier indications for a non-zero θ_{13} mixing angle from the observation of electron neutrino appearance on a muon neutrino beam at the accelerator oscillation experiments MINOS [228] and T2K [79]. Together with the hints from the solar and atmospheric neutrino data samples, this gave 3 and 4σ indications of non-zero θ_{13} , depending on the treatment of short-baseline reactor data used in the global oscillation analysis [235, 236]. By including the recent measurements of reactor anti-neutrino disappearance reported by the DC [232], DYB [78] and RENO data [233] together with the latest results of the MINOS [228] and T2K [237] experiments, the significance becomes overwhelming.

4.5

Global Neutrino Oscillation Analysis

Solar neutrino oscillation analyses were performed including the available data samples⁷⁾ and taking into account both statistical errors and systematic uncertainties such as those of the eight solar neutrino fluxes, neutrino production distributions and solar density profile. In the simulation of the production and propagation of neutrinos in the Sun, Ref. [83] takes into account the most recent update of the SSM [239], choosing the low metallicity model labelled as AGSS09. The impact of the choice of a particular solar model over the neutrino oscillation analysis has been critically discussed in the arXiv updated version of Ref. [240].

Reactor anti-neutrinos are produced by the fission of the ^{235}U , ^{239}Pu , ^{241}Pu and ^{238}U isotopes. Each fissile isotope contributes to the total reactor neutrino flux and fuel content with a certain fission fraction f^l . They are detected via the inverse beta decay process, looking for a delayed coincidence between the positron annihilation and the neutron capture in the target material. The window of positron energy covered by the three experiments described above ranges from 0.7 to 12 MeV approximately. The total number of events expected at the i th detector coming from the r th reactor in a given experiment is written as

$$N_{i,r} = \frac{N_p P_{th}^r}{4\pi L_{ir}^2 \langle E_{fis} \rangle} \epsilon_i \int_0^\infty dE_\nu \Phi^r(E_\nu) \sigma_{\text{IBD}}(E_\nu) P(E_\nu, L_i), \quad (4.19)$$

where N_p is the number of protons in the target volume, P_{th}^r is the total reactor power, ϵ_i denotes the efficiency of the detector and $\langle E_{fis} \rangle = \sum_l f^l E_{fis}^l$ is the average energy released per fission, calculated from the individual fission fractions f^l and the energy release per fission for a given isotope l taken from Ref. [241]. For the anti-neutrino flux prediction $\Phi^r(E_\nu)$, one uses the recent parameterization given in Ref. [242] as well as the new normalization for reactor anti-neutrino fluxes updated in Ref. [238]. The inverse beta decay cross section $\sigma_{\text{IBD}}(E_\nu)$ is taken from Ref. [243]. Finally, for the neutrino propagation factor $P(E_\nu, L_{ir})$, one uses the

⁷⁾ Here we will not include the recent anomalies observed in neutrino experiments and the latest astrophysical data which might suggest the existence of light sterile neutrinos [238].

full three-neutrino disappearance probability. The distance between the reactor and detector L_{ir} is also used to correct the total anti-neutrino flux at the detector site. In order to minimize the dependence upon the predicted normalization of the anti-neutrino spectrum, one takes the total rate of expected events at the far detector/s in the presence of oscillations over the no-oscillation prediction. This way, the statistical analysis is free of correlations among the different reactor data samples, since the relative measurements do not rely on flux predictions.

As far as atmospheric neutrino fluxes are concerned, one has detailed three-dimensional calculations given in [221], which can be employed to perform a global fit of the oscillation parameters [244, 245]. Alternatively, one may use directly the official Super-Kamiokande analysis of atmospheric neutrino data within the one-mass scale approximation, given in Ref. [246]. This choice is adopted in the analysis of Ref. [83], and results from the three phases of the Super-Kamiokande experiment are included. Concerning the long-baseline data, one takes into account the most recent results from the MINOS and T2K long-baseline experiments presented at the Neutrino 2012 Conference, in the appearance and disappearance channels for both experiments as well as the neutrino and anti-neutrino data for MINOS. These new long-baseline results give improvements with respect to the previous MINOS and T2K data [79, 227–230]. On one hand, the new results on $\nu_\mu \rightarrow \nu_e$ appearance searches allow a better determination of the θ_{13} mixing angle, although its current determination is fully dominated by the DYB reactor data. On the other hand – and here lies the most relevant implication of the new long-baseline data – they show a preference for a non-maximal atmospheric mixing angle θ_{23} in the ν_μ and $\bar{\nu}_\mu$ channels.

In the global analysis of neutrino oscillation parameters, one combines the recent reactor data from DC [232], DYB [78, 247] and RENO data [233] with all the remaining relevant experiments, as follows: the accelerator results including the latest MINOS [228] and T2K [237] experiments; data from all the three phases of the Super-Kamiokande solar [198–200] and atmospheric experiment [246]; the three phases from the Sudbury Neutrino Experiment SNO [202, 203] solar neutrino measurements; the Borexino [207] data and previous radiochemical rate measurements [33, 196, 197].

4.6

Global Fit Results for Neutrino Oscillation Parameters

The results for the neutrino oscillation parameters obtained in the global analysis in [83] are summarized below.

The results obtained for $\sin^2\theta_{13}$ and δ are summarized in Figure 4.12. In the upper panels, the $\Delta\chi^2$ profile is given as a function of $\sin^2\theta_{13}$ for normal (left panel) and inverted (right panel) neutrino mass hierarchies. The solid dark line corresponds to the result obtained from the combination of all the data samples, while the others correspond to the individual reactor data samples and the combination of the long-baseline MINOS and T2K appearance and disappearance data, as indicated. One sees from the constraints on $\sin^2\theta_{13}$ coming from the different

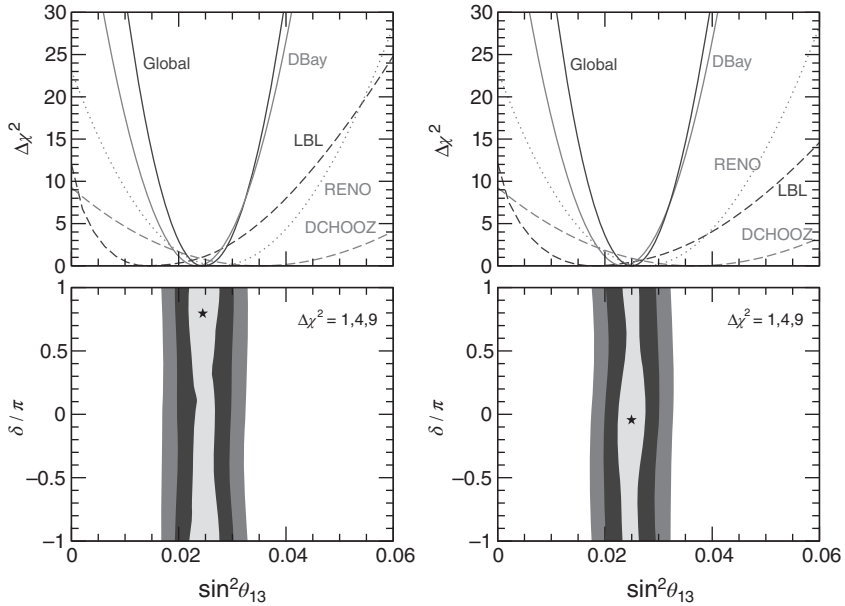


Figure 4.12 Upper panels: $\Delta\chi^2$ as a function of $\sin^2\theta_{13}$ from the analysis of the total event rate in Daya Bay (solid light line), RENO (dotted line) and Double Chooz (dashed light line) as well as from the analysis of long-baseline (dashed dark line) and global neutrino data (solid dark line). Except for the case of the global fit, here we have

fixed the remaining oscillation parameters to their best fit values. Lower panels: contours of $\Delta\chi^2 = 1, 4, 9$ in the $\sin^2\theta_{13} - \delta$ plane from the global fit to the data. We minimize over all undisplayed oscillation parameters. Left (right) panels are for normal (inverted) neutrino mass hierarchy. (Adapted from Ref. [83].)

data samples separately that, as expected, the global constraint on θ_{13} is dominated by the recent DYB measurements. For both neutrino mass hierarchies, we find that the 3σ indication for $\theta_{13} > 0$ obtained previously [236] due mainly to the first indications observed by MINOS and T2K is now overwhelmingly confirmed as a result of the recent reactor data. Thus, in the global fit one obtains a $\Delta\chi^2 \sim 104$, resulting in a 10.2σ exclusion of $\theta_{13} = 0$ for both mass hierarchies. The lower panels of Figure 4.12 give the contours of $\Delta\chi^2 = 1, 4, 9$ in the $\sin^2\theta_{13} - \delta$ plane from the global fit to the neutrino oscillation data. The best fit points are

$$\sin^2\theta_{13} = 0.0246, \quad \delta = 0.80\pi \quad (\text{normal hierarchy}), \quad (4.20)$$

$$\sin^2\theta_{13} = 0.0250, \quad \delta = -0.03\pi \quad (\text{inverted hierarchy}). \quad (4.21)$$

Note that no ‘preferred region’ for the CP phase δ remains at $\Delta\chi^2 = 1$.⁸⁾ For this reason, one marginalizes over the CP phase δ (and all other oscillation parameters), obtaining for the best fit 1σ errors and the significance for $\theta_{13} > 0$:

⁸⁾ Within the approximations in [246], the sensitivity to δ comes only from long-baseline neutrino data.

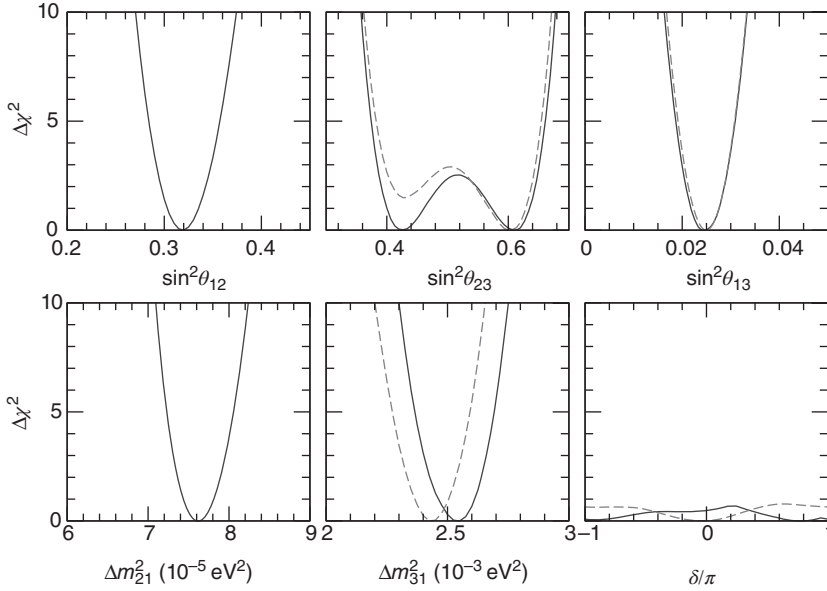


Figure 4.13 $\Delta\chi^2$ profiles as a function of all the neutrino oscillation parameters $\sin^2\theta_{12}$, $\sin^2\theta_{23}$, $\sin^2\theta_{13}$, Δm_{21}^2 , Δm_{31}^2 and δ . For the central and right panels, the solid

lines correspond to the case of normal mass hierarchy, while the dashed lines correspond to the results for the inverted mass hierarchy. (Adapted from Ref. [83].)

$$\begin{aligned} \sin^2\theta_{13} &= 0.0246^{+0.0029}_{-0.0028}, & \Delta\chi^2 &= 103.5 \text{ (10.2}\sigma\text{)} & \text{(normal),} \\ \sin^2\theta_{13} &= 0.0250^{+0.0026}_{-0.0027}, & \Delta\chi^2 &= 104.7 \text{ (10.2}\sigma\text{)} & \text{(inverted).} \end{aligned} \quad (4.22)$$

Besides θ_{13} and δ , from the global analysis of neutrino data we also re-calculated the best fit values and ranges allowed for all the other neutrino oscillation parameters. Our results are summarized in Figure 4.13. A detailed summary table of three-neutrino oscillation parameters for normal and inverted neutrino mass hierarchies is given in Ref. [83].

The most striking feature in Figure 4.13 is that the ‘solar’ angle is large, quite different from its quark analogue, namely the Cabibbo angle. Likewise, the ‘atmospheric’ angle is quite different from the corresponding Kobayashi–Maskawa mixing parameter. In Figure 4.14, we show the allowed regions for the solar (a) and atmospheric (b) neutrino oscillation parameters from the global analysis in Ref. [83], the latter corresponding to the case of normal neutrino mass hierarchy (solid lines in middle panels of Figure 4.13). Comparing with previous results, one sees that the inclusion of the new reactor and long-baseline data does not have a strong impact on the determination of the solar neutrino oscillation parameters, as these are already pretty well determined by solar and KamLAND reactor data.

In contrast, the precision in the determination of the atmospheric mass-squared splitting parameter Δm_{31}^2 improves thanks to the new long-baseline neutrino data. Thus, at 3σ , one finds approximately an 8% accuracy in the determination of Δm_{31}^2 ,

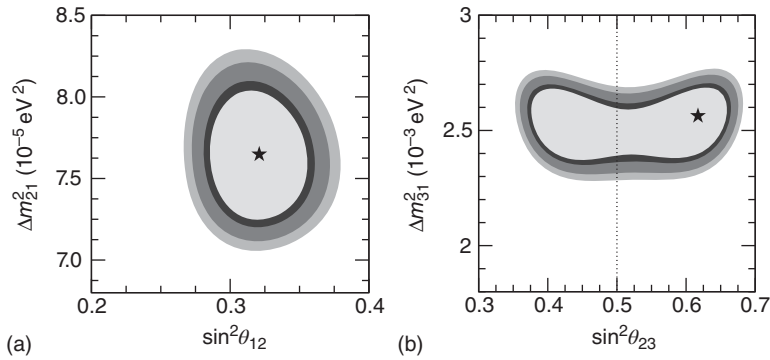


Figure 4.14 Regions for the solar (a) and atmospheric (b) neutrino oscillation parameters allowed at 90% CL, 95% CL, 99% CL and 3σ by the global analysis in Ref. [83].

compared with the previous 12% accuracy obtained in [236] at 3σ . For the atmospheric mixing angle, there is now some rejection for maximal values of θ_{23} , as can be seen in Figure 4.13. Note that the new disappearance data from MINOS shows a preference for non-maximal values of θ_{23} . Owing to the smallness of the associated matter effects in MINOS, these data are octant-symmetric in θ_{23} . However, when we then include atmospheric data in the global analysis, differences in the determination of θ_{23} arise. Hence the interplay with long-baseline neutrino appearance and reactor anti-neutrino data breaks the octant degeneracy, leading to a small preference for values of θ_{23} smaller than $\pi/4$. This is seen in the left panels of Figure 4.15, where we have plotted the allowed regions in the $\sin^2\theta_{23} - \sin^2\theta_{13}$ plane from the combination of long-baseline (MINOS and T2K) with solar + KamLAND. These data samples prefer θ_{23} values in the first octant, and the same holds for the case when new reactor data are included, see middle panels in Figure 4.15.

Note that, while the preference for non-maximal values of the atmospheric mixing angle comes directly from the new MINOS data, the choice of a particular octant comes from the interplay of the long-baseline neutrino oscillation data with the reactor and atmospheric data. For a critical comparison with the other recent global neutrino oscillation analyses in Refs [244, 245], see Ref. [83]. The indicated points denote best fit values, while the narrower ranges correspond to 1σ and the wider ones to 3σ intervals. At the moment of writing, we need more information in order to decide the octant of θ_{23} .

4.7

Summary and Outlook

In this chapter, we described the present status of neutrino oscillations through a global fit to world data, giving a concise determination of the parameters governing neutrino oscillations. Thanks to a variety of complementary solar neutrino and KamLAND reactor experiments (left panel of Figures 4.16 and 4.17),

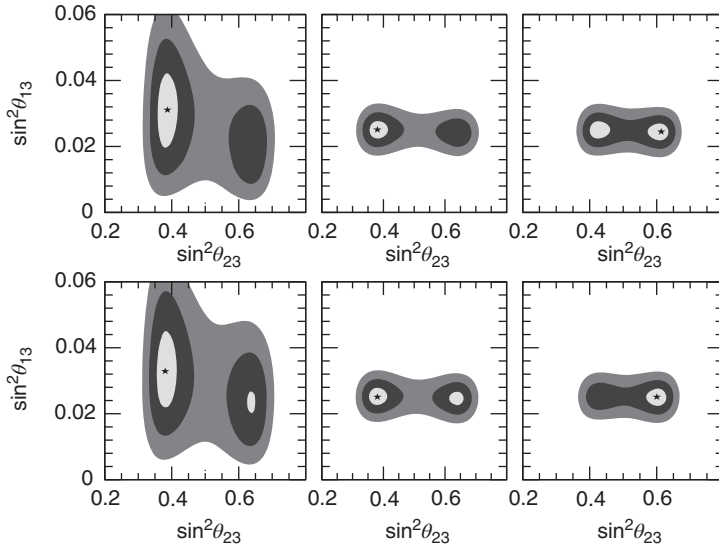


Figure 4.15 Upper panels: contour regions with $\Delta\chi^2 = 1, 4, 9$ in the $\sin^2\theta_{23}$ – $\sin^2\theta_{13}$ plane from the analysis of long-baseline (MINOS and T2K) + solar + KamLAND data (left panel), long-baseline + solar + KamLAND + new Double Chooz, Daya Bay and

RENO reactor data (middle panel) and the global combination (right panel) for normal hierarchy. Lower panels: same but for (inverted) neutrino mass hierarchy. (Adapted from Ref. [83].)

the parameters governing solar neutrino oscillations have converged to a unique region, shown in the top-right part of Figure 4.17. This, in particular, excludes the previously allowed ‘just-so’ solutions where the oscillations take place *in vacuo* with $\Delta m_{21}^2 \sim 10^{-10} \text{eV}^2$, as well as the small angle and LOW solutions [248] as seen in Figure 4.17. The small panels summarize the complementarity between ‘underground’ and ‘laboratory’ experiments in the determination of solar and atmospheric neutrino oscillation parameters, while the last one gives the current

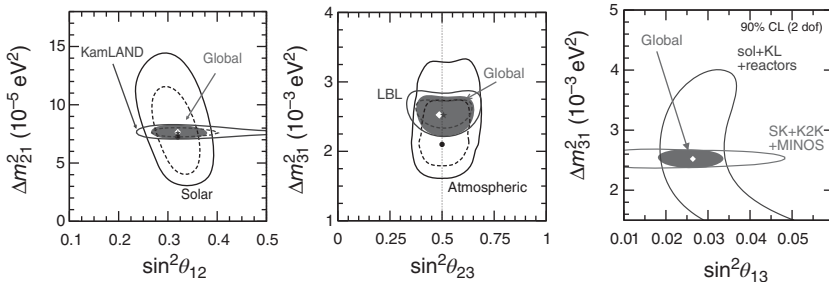


Figure 4.16 Status of neutrino oscillations from the global fit in [83]. The left panel gives a zoom of the solar oscillation parameters, while the others refer to the

atmospheric and reactor sectors, for normal hierarchy. Solid and dashed contours indicate 3σ and 90%CL, respectively. (Courtesy of M. Tortola.)

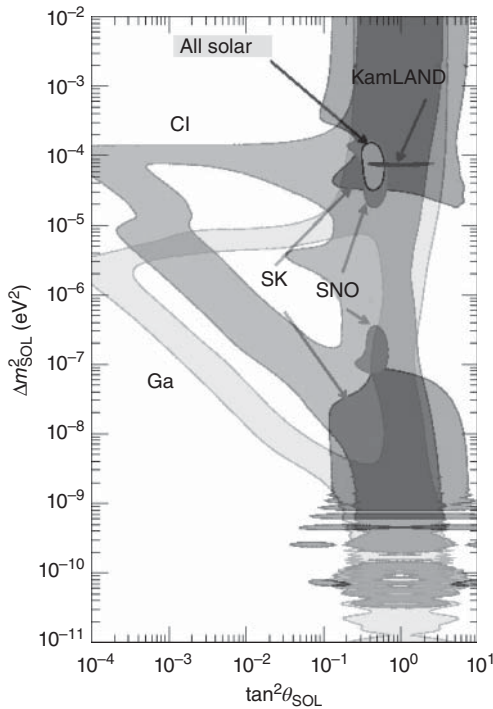


Figure 4.17 Grand view of the progress achieved in the determination of solar oscillation parameters over the last 15 years or so. (Courtesy of M. Tortola.)

precise determination of θ_{13} which governs CP violation in neutrino oscillations to be probed in the next generation of accelerators.

Another way to summarize is given in Figure 4.18, which displays a schematic sum-up of the results of the neutrino oscillation global fits, for the case of normal mass hierarchy. In order to guide the eye, we have also indicated by the vertical dashed lines the predictions of the tri-bimaximal mixing pattern [249], see Chapter 16.

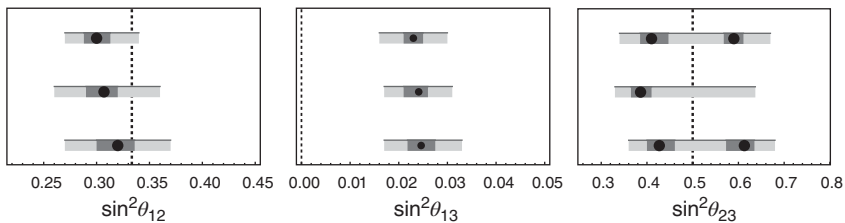


Figure 4.18 In each panel, the three bands refer to three recent global neutrino data analysis, namely [245] (top), [244] (medium) and [83] (bottom) for normal mass hierarchy. The lengths of the bands correspond to 1σ and 3σ .

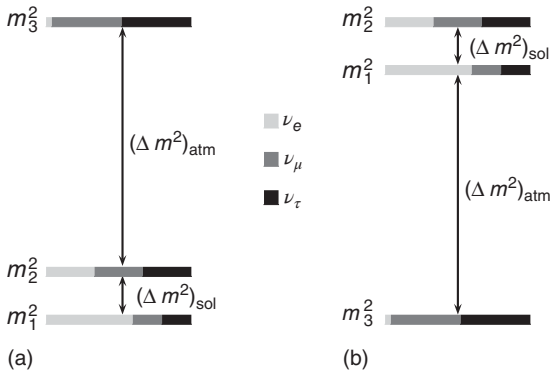


Figure 4.19 (a,b) Normal and inverted neutrino mass hierarchies. Here we denote with 'atm' and 'sol' the atmospheric and solar squared mass splittings, respectively, indicating also the best flavour content of each mass eigenstate.

On the other hand, an adequate oscillation picture may be realized within two types of neutrino mass spectra, namely normal or inverted, as illustrated in Figure 4.19. During proof-reading of this book new results were presented at the Neutrino-2014 conference. These include reactor anti-neutrino disappearance data of Daya Bay and RENO, together with latest T2K and MINOS disappearance and appearance data. Also new results from the Super-K collaboration. With their inclusion one finds an increased sensitivity to the CP phase, thanks to the interplay between accelerator and reactor data. For details see D.V. Forero, M. Tortola, J.W.F. Valle, Phys. Rev. D90 (2014)093006 [e-Print: arXiv:1405.7540].

The discovery of oscillations has fundamental importance, as it provides a proof of the need for extending the standard model in order to incorporate neutrino masses. So fundamentally profound is this conclusion that it requires us to be specially cautious in regard to the robustness of the oscillation interpretation, an issue to which we turn in the next chapter.

4.8

Problems for Chapter 4

4.1 Consider the process that creates one neutrino with flavour α , together with the corresponding charged lepton

$$A \rightarrow B + l_{\alpha}^{+} + \nu_{\alpha}, \quad (4.23)$$

where A, B are nuclei. The effective Lagrangian describing this interaction can be written as

$$\mathcal{L}_{A \rightarrow B} = \bar{\nu}_k \gamma^{\mu} P_L l_{\alpha} U_{\alpha k}^{*} J_{\mu}^{A \rightarrow B} + \text{h.c.} \quad (4.24)$$

Then, the second quantized state with flavour α is

$$|\nu_{\alpha}\rangle \propto \sum_{k=1}^3 |\nu_k\rangle \langle \nu_k, l_{\alpha}^{+} | \mathcal{L}_{A \rightarrow B} | 0 \rangle. \quad (4.25)$$

Using now the definition

$$\langle \nu_k, l_\alpha^+ | = \langle 0 | A_k(p_1) d(p_2), \quad (4.26)$$

where $A_k(p_1)$ and $d(p_2)$ are the annihilation operators for neutrinos and positively charged leptons, respectively, and the plane wave expansion of the operators in $\mathcal{L}_{A \rightarrow B}$, show that

$$\langle \nu_k, l_\alpha^+ | \mathcal{L}_{A \rightarrow B} | 0 \rangle \propto U_{\alpha k}^* \quad (4.27)$$

and therefore the correctly normalized states are given by

$$|\nu_\alpha\rangle = \sum_{k=1}^3 U_{\alpha k}^* |\nu_k\rangle \quad (4.28)$$

in agreement with Eq. (4.4).

4.2 Consider the neutrino oscillation probability given in Eq. (4.5). For three families, there is only one independent imaginary part

$$\Im\{U_{\alpha i}^* U_{\alpha j} U_{\beta i} U_{\beta j}^*\},$$

which is responsible for CP violation in neutrino oscillations. Calculate this invariant within the symmetrical parameterization and compare it with the PDG presentation

$$\begin{aligned} J_{CP} &= \Im\{U_{e1}^* U_{\mu 3}^* U_{e3} U_{\mu 1}\} \\ &= \begin{cases} \frac{1}{8} \sin 2\theta_{12} \sin 2\theta_{23} \sin 2\theta_{13} \cos \theta_{13} \sin \delta & \text{(PDG),} \\ \frac{1}{8} \sin 2\theta_{12} \sin 2\theta_{23} \sin 2\theta_{13} \cos \theta_{13} \sin(\phi_{13} - \phi_{12} - \phi_{23}) & \text{(symm),} \end{cases} \end{aligned} \quad (4.29)$$

with δ given by the PDG conventions [21].

4.3 For Majorana neutrinos, one can have a novel type of neutrino oscillation, violating lepton number by two units, as illustrated in Figure 4.20.

Calculate the $\nu_\alpha \rightarrow \bar{\nu}_\beta$ oscillation probability for ultra-relativistic neutrinos

$$P(\nu_\alpha \rightarrow \bar{\nu}_\beta) = \frac{1}{E^2} \left| \sum_j U_{\alpha j} U_{\beta j} m_j e^{-iE_j t} \right|^2 \quad (4.30)$$

and show that the Majorana CP phase appears explicitly and hence is a physical parameter. Hint: it is enough to use the symmetrical parameterization of the lepton mixing matrix for the simplest case of two neutrinos, Eq. (3.26).

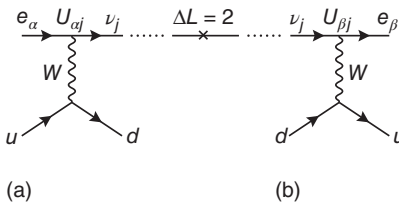


Figure 4.20 Schematic illustration of neutrino oscillations *in vacuo* (a) and matter (b).

4.4 Show that, within the adiabatic regime of slowly varying matter densities, the two-neutrino survival probability can be approximated by Parke's formula [250]

$$P(\nu_e \rightarrow \nu_e) = \frac{1}{2}[1 + \cos 2\theta \cos 2\theta_m], \quad (4.31)$$

where θ_m is the effective mixing angle at the neutrino production point in the Sun. In this case, the mixing angle in matter is given by the MSW expression, Eq. (4.10).

